Metrol. Meas. Syst., Vol. 32 (2025), No. 2
DOI: 10.24425/mms.2025.154339

METROLOGY AND MEASUREMENT SYSTEMS
Index 330930, ISSN 0860-8229
www.metrology.wat.edu.pl

SENSORLESS CONTROL OF PERMANENT MAGNET SYNCHRONOUS MOTOR BASED ON INTERACTING MULTIPLE MODELS EXTENDED KALMAN FILTER

Yong Li, Jiexin An, Han Hu, Xing Xu

Automotive Engineering Research Institute, Jiangsu University, Zhenjiang 212013,China (✉ *liyongthinkpad@outlook.com*)

Abstract

Aiming at the problems of low estimation accuracy and narrow application range of sensorless control caused by inverter nonlinearity and motor parameter error, this paper studies a sensorless control technology of permanent magnet synchronous motor based on interactive multi-model extended Kalman filter algorithm to realize high-precision and high-performance sensorless control of permanent magnet synchronous motor. Firstly, considering the influence of inverter nonlinearity, the mathematical model of PMSM including inverter disturbance voltage is established. Secondly, an interactive multi-model extended Kalman filter observer is designed based on this model to achieve high-precision sensorless control of PMSM. Thirdly, the nonlinear disturbance voltage of the inverter is fed back to the control system for dead-time compensation, thus eliminating the voltage disturbance caused by the dead-time effect. Finally, simulation experiments and dual-motor towing experiments demonstrate the efficacy of the interactive multi-model extended Kalman filter sensorless control algorithm in mitigating the effects of dead time. The results indicate that the proposed algorithm exhibits high precision in speed and angle estimation, robust anti-disturbance capabilities, and excellent overall performance.

Keywords: permanent magnet synchronous motor, sensorless control, extended Kalman filter algorithm, inverter nonlinearity, dead-time compensation.

1. Introduction

The in-wheel motor drive system is composed of in-wheel motors, drive controllers, and Hall position sensors. These components are installed in a limited in-wheel space and have highly integrated characteristics [1]. The occurrence of road impact, vibration, motor temperature rise, inverter dead zone, and other factors will not only result in a variation in the sensitivity of the Hall position sensor, temperature drift, and other complications, but also lead to an increase in the volume of the motor, system cost, and failure rate [2]. Therefore, it is necessary to study the sensorless control of the in-wheel motor and realize the software measurement of the rotor position, speed, and other information of the in-wheel motor through the control algorithm. This approach is intended to address the limitations of the traditional Hall position sensor [3-4].

In addition to the salient pole effect method suitable for the zero-low speed stage [5], the sensorless control technology also includes the fundamental wave model method suitable for the medium-high speed stage [6]. The fundamental wave model of a permanent magnet in-wheel motor at high speed contains abundant signals such as voltage and current, and the speed [7] and position information [8] of the in-wheel motor can be obtained by the fundamental wave model method. However, this method is very dependent on the motor speed, and the signal-to-noise ratio of the back EMF is low at low speeds [9]. Currently, the fundamental wave model method mainly includes the *electromagnetic force* (EMF) method [10], flux linkage estimation method [11], state observer method [12], artificial neural network method [13], and so on. Zhang *et al.* [14] propose a discrete rotor position offset compensation method for permanent

Article history: received July 24, 2024; revised October 24, 2024; accepted November 6, 2024; available online April 11, 2025.

magnet synchronous motors based on back-EMF, and design an adaptive disturbance observer with multi-parameter estimation to improve the compensation accuracy and algorithm execution efficiency. However, this method relies too much on the accurate discrete back-EMF model. Ye *et al.* [15] study a sensorless control scheme based on *iterative flux sliding mode observer* (IFSMO), which expands the state equation of the permanent magnet synchronous motor with the flux of the permanent magnet synchronous motor, and estimates the speed and position of the rotor by using the flux rather than the back electromotive force information. This method reduces the chattering in the estimation results, but it takes a lot of time to adjust the observer gain. Yang *et al.* [16] design a speed sensorless control strategy combining an improved *sliding mode observer* (SMO) and a *phase-locked loop* (PLL). The improved sliding mode observer adopts the switching function of the double boundary layer structure to reduce the high-frequency vibration and improve the speed tracking performance. However, this method has poor tracking performance in the strong disturbance region. Remzi *et al.* [17] use the artificial neural network method to estimate the rotor speed of the brushless DC motor, and combine with an extended Kalman filter estimator to achieve a new hybrid speed estimator. However, this method is highly dependent on the network model and cannot guarantee the accuracy of the actual estimation results.

In practical applications, the inverter dead time [18] and parameter identification problems [19] will have a negative impact on the rotor position estimation, thereby reducing the control performance. To achieve high-performance sensorless control considering inverter disturbance voltage compensation and parameter identification, this paper proposes a position sensorless control algorithm based on the *Interactive Multiple Models Extended Kalman Filter* (IMM-EKF). Compared with the existing methods, the main advantage of the IMM-EKF algorithm is that it can deal with nonlinear and non-Gaussian systems, and can use multiple different motion models to describe the motion of the system, thereby improving the accuracy of the estimation. In addition, the IMM-EKF algorithm can also adaptively adjust the weight of each EKF filter according to different requirements and actual conditions to adapt to different working conditions.

The principal contributions of this paper are as follows:

(1) A mathematical model of the *permanent magnet synchronous motor* (PMSM) including the inverter disturbance voltage is established, taking into account the nonlinear factors of the inverter.

(2) A position sensorless control algorithm based on an interacting multiple model extended Kalman filter is proposed. This greatly improves the estimation accuracy of the speed and angle and the operating range of the sensorless control.

(3) To validate the proposed interactive multi-model extended Kalman filter position sensorless control algorithm, a dual-motor towing test bench is built in the laboratory. The speed and angle estimation accuracy of the proposed algorithm are verified by simulation experiments, and the anti-disturbance ability and robustness of the algorithm under different working conditions are verified by using the built dual-motor towing test bench.

The structure of this paper is as follows. Firstly, in the second section, the influence of inverter nonlinearity is analyzed and the mathematical model of a permanent magnet synchronous motor with dead-time disturbance voltage is established. In the third section, the principle of interacting multiple model algorithm is introduced, and a position sensorless control observer based on interacting multiple model extended Kalman filter is designed. In the fourth section, the simulation experiment based on Matlab and the physical bench experiment of double motor towing is designed to verify the effectiveness of the interactive multi-model extended Kalman filter sensorless control algorithm. The fifth section is the conclusion of this paper.

2. Mathematical model of PMSM considering inverter nonlinearity

The average voltage of each phase in a switching cycle Ts should be equal to the reference voltage, as illustrated in Fig. 1(a). The ideal voltage value is no longer consistent with the actual voltage value in the presence of the dead zone effect, as depicted in Fig. 1(b) [20].

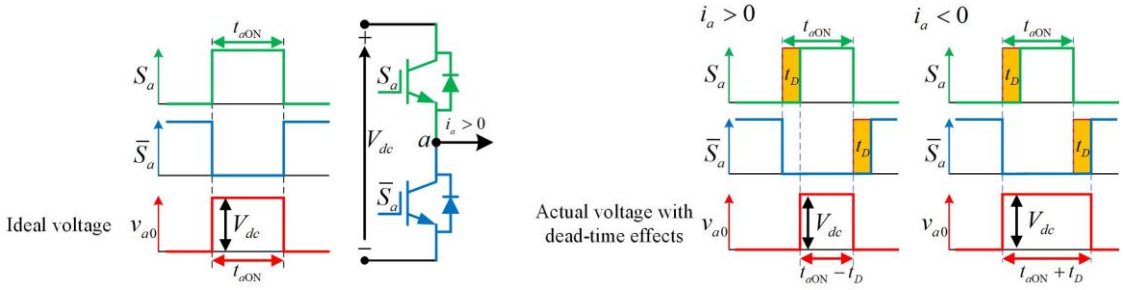

(a) Ideal reference voltage (b) Actual reference voltage

Fig. 1. Schematic diagram of ideal and actual reference voltages

At this present time, the discrepancy between the reference value of the *a*-phase voltage and the actual value is as follows:

$$u_{a,err} = V_{dead} \cdot \mathrm{sgn}(i_a) \tag{1}$$

$$V_{dead} = \frac{T_{dead} + T_{on} - T_{off}}{T_s}\left(V_{dc} - V_{sat} + V_d\right) + \frac{V_{sat} + V_d}{2} \tag{2}$$

In the formula, V_{dead} represents the voltage drop resulting from VSI nonlinearity, T_{dead} denotes the dead time, T_{on} and T_{off} are the turn-on and turn-off delay of the switching tube, respectively, V_{sat} and V_d are the voltage drop of the switching tube and the freewheeling diode, respectively, V_{dc} is the bus voltage, sgn(·) is the sign function.

Due to the nonlinear characteristics of the inverter output voltage, including the dead-time effect, there is an error between the reference values u_d^* and u_q^* and the actual values u_d and u_q. This voltage error is regarded as a disturbance in the control system. From the dead-time voltage model, which considers the nonlinear factors of the inverter, the voltage equation of the permanent magnet synchronous motor is:

$$\begin{cases} u_d^* - V_{dead}\, D_d = R_s i_d + L_s \dfrac{di_d}{dt} - L_s i_q \omega_e \\ u_q^* - V_{dead}\, D_q = R_s i_q + L_s \dfrac{di_q}{dt} + L_s i_d \omega_e + \omega_e \psi_s \end{cases} \tag{3}$$

Where i_d and i_q are *d*-axis and *q*-axis stator currents respectively, u_d and u_q are *d* and *q*-axis stator voltages, respectively. ω_e is the electromechanical angular velocity, R_s, L_s, and Ψ_s are the stator resistance, inductance, and rotor flux of the motor, respectively. V_{dead} represents the disturbance voltage, taking into account the nonlinear factors of the inverter. D_d and D_q are interval piecewise functions about θ_e, u_d* and u_q* are the reference values of the output voltage of the inverter.

The presence of the disturbance voltage V_{dead} has the potential to impact the accuracy of the sensorless control algorithm [21]. To enhance the precision of the motor sensorless control, it is essential to accurately estimate and compensate for the V_{dead} value.

3. Sensorless control observer design of PMSM based on IMM-EKF

3.1. Principle of IMM-EKF algorithm

The IMM algorithm is a multi-model tracking algorithm based on multiple filters, which can also be referred to as a soft switching algorithm. The flow chart of the IMM algorithm is shown in Fig. 2. The detailed calculation process of the IMM algorithm is usually recursively carried out in four steps, as follows:

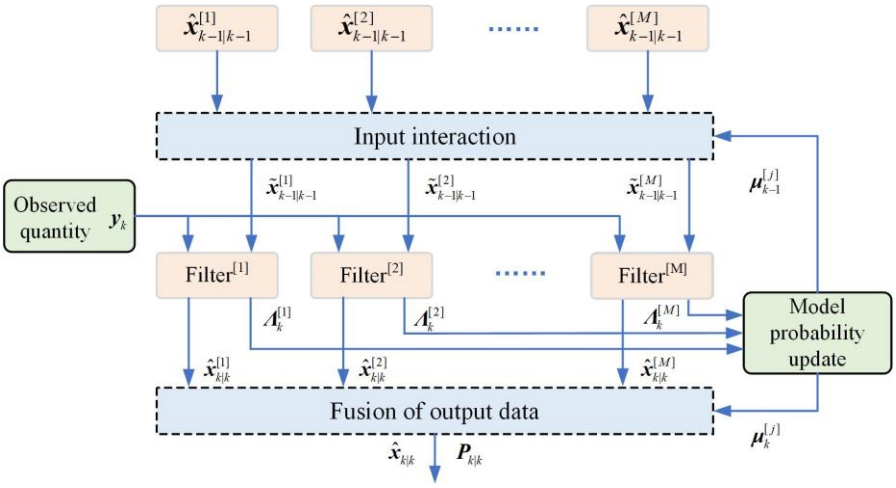

Fig. 2. The flow chart of IMM algorithm

Step 1: Interaction of input model

The interaction of the input model is to mix the state estimate $\hat{\boldsymbol{x}}_{k-1|k-1}^{[i]}$ of the system estimated at the previous moment with the probability $\boldsymbol{\mu}_{k-1}^{[j]}$ of each filter model at the previous moment, and solve to obtain the initial mixed state estimate $\tilde{\boldsymbol{x}}_{k-1|k-1}^{[j]}$ and the initial mixed covariance estimate $\tilde{\boldsymbol{P}}_{k-1|k-1}^{[j]}$ of the current cycle. The specific calculation formula is as follows:

$$\tilde{\boldsymbol{x}}_{k-1|k-1}^{[j]} = \sum_{i=1}^{M} \hat{\boldsymbol{x}}_{k-1|k-1}^{[i]} \boldsymbol{\mu}_{k-1|\,k-1}^{[i\to j]} \tag{4}$$

$$\tilde{\boldsymbol{P}}_{k-1|k-1}^{[j]} = \sum_{i=1}^{M} \boldsymbol{\mu}_{k-1|\,k-1}^{[i\to j]} \cdot [(\hat{\boldsymbol{x}}_{k-1|k-1}^{[i]} - \tilde{\boldsymbol{x}}_{k-1|k-1}^{[j]}) \cdot (\hat{\boldsymbol{x}}_{k-1|k-1}^{[i]} - \tilde{\boldsymbol{x}}_{k-1|k-1}^{[j]})^{T}] \tag{5}$$

$$\boldsymbol{\mu}_{k-1|\,k-1}^{[i\to j]} = (1/\bar{c}_j)\, p^{[i\to j]} \boldsymbol{\mu}_{k-1}^{[i]} \tag{6}$$

$$\bar{c}^{[j]} = \sum_{i=1}^{M} p^{[i\to j]} \boldsymbol{\mu}_{k-1}^{[i]} \tag{7}$$

Where $\tilde{\boldsymbol{x}}_{k-1|k-1}^{[j]}$ and $\tilde{\boldsymbol{P}}_{k-1|k-1}^{[j]}$ are the initial mixed state estimation and initial mixed covariance estimation of the current cycle of model *j*, respectively. $\hat{\boldsymbol{x}}_{k-1|k-1}^{[i]}$ is the state estimation of any model system estimated at the previous time. $\boldsymbol{\mu}_{k-1|\,k-1}^{[i\to j]}$ is the mixing probability of the previous time, that is, the estimation of the previous cycle is given the weight of each filter at the beginning of the current cycle. $p^{[i\to j]}$is the mixing probability of the transition from model *i* to model *j*, $\boldsymbol{\mu}_{k-1}^{[i]}$ is the probability of model *i* at time *k*-1, and $\bar{c}_j$ is the normalized constant of the

predicted probability of model j, $[i \to j]$ represents the transition from model i to model j, $\tilde{*}$ represents the initial mixing estimate, and $\hat{*}$ represents the estimate.

Step 2: Filtering of the filter

In this part, this paper selects the EKF filter to expand the design of the filtering link. Firstly, the initial mixed state estimate $\tilde{x}_{k-1|k-1}^{[j]}$, the initial mixed covariance estimate $\tilde{\boldsymbol{P}}_{k-1|k-1}^{[j]}$, and the measurement equation $\boldsymbol{y}_k^{[j]}$ of the current cycle model j obtained by step 1 are used to obtain the new current predicted state estimate and the filter covariance according to the EKF filtering process. Secondly, the EKF filtering process can predict and update the IMM-EKF algorithm according to the framework of the Kalman filter algorithm, and calculate the state estimation and uncertainty.

Specifically, taking model j as an example, the state estimation and uncertainty calculation formulas in the prediction stage are as follows:

$$\hat{\boldsymbol{x}}_{k|k-1}^{[j]} = f^{[j]}(\tilde{\boldsymbol{x}}_{k-1|k-1}^{[j]}, \boldsymbol{u}_k^{[j]}) \tag{8}$$

$$\boldsymbol{P}_{k|k-1}^{[j]} = \boldsymbol{F}_{k-1}^{[j]} \tilde{\boldsymbol{P}}_{k-1|k-1}^{[j]} (\boldsymbol{F}_{k-1}^{[j]})^T + \boldsymbol{Q}_k^{[j]} \tag{9}$$

Where $\boldsymbol{F}_{k-1}^{[j]}$ is the Jacobian matrix of $f(x,u)$ at $\hat{x}$, and $\boldsymbol{Q}_k^{[j]}$ is the process noise covariance matrix of model j.

The formula for state estimation and uncertainty calculation in the update phase is as follows:

$$K_k^{[j]} = \boldsymbol{P}_{k-1|k-1}^{[j]} (\boldsymbol{G}_k^{[j]})^T [\boldsymbol{G}_k^{[j]} \boldsymbol{P}_{k-1|k-1}^{[j]} (\boldsymbol{G}_k^{[j]})^T + \boldsymbol{R}_k^{[j]}]^{-1} \tag{10}$$

$$\hat{\boldsymbol{x}}_{k|k}^{[j]} = \hat{\boldsymbol{x}}_{k|k-1}^{[j]} + K_k^{[j]} (\boldsymbol{y}_k^{[j]} - g^{[j]}(\hat{\boldsymbol{x}}_{k|k-1}^{[j]})) \tag{11}$$

$$\boldsymbol{P}_{k|k}^{[j]} = (\boldsymbol{I}^{[j]} - K_k^{[j]} \boldsymbol{G}_k^{[j]}) \boldsymbol{P}_{k|k-1}^{[j]} \tag{12}$$

Where $K_k^{[j]}$ is the Kalman gain coefficient of model j, $\boldsymbol{G}_k^{[j]}$ is the Jacobian matrix of $g^{[j]}(x)$ at $\hat{\boldsymbol{x}}_{k|k-1}^{[j]}$, $\boldsymbol{R}_k^{[j]}$ is the observation noise covariance matrix of model j, $\boldsymbol{y}_k^{[j]}$ is the current observation data of model j, and $\boldsymbol{I}^{[j]}$ is the unit matrix.

Step 3: Update of model probability

Taking model j as an example, the update of model probability $\boldsymbol{\mu}_k^{[j]}$ in the IMM algorithm flow usually adopts the following formula.

$$\boldsymbol{\mu}_k^{[j]} = \frac{1}{c} \boldsymbol{\Lambda}_k^{[j]} \sum_{i=1}^{M} p^{[i \to j]} \boldsymbol{\mu}_{k-1}^{[i]} = \frac{1}{c} \boldsymbol{\Lambda}_k^{[j]} \overline{c}^{[j]} \tag{13}$$

$$c = \sum_{i=1}^{M} \boldsymbol{\Lambda}_k^{[j]} \overline{c}^{[j]} \tag{14}$$

$$\boldsymbol{\Lambda}_k^{[j]} = \frac{1}{\sqrt{(2\pi)^n \left| s_k^{[j]} \right|}} \exp\left\{ -\frac{1}{2} \boldsymbol{d}_k^{[j]} \left(\boldsymbol{S}_k^{[j]} \right)^{-1} \left(\boldsymbol{d}_k^{[j]} \right)^T \right\} \tag{15}$$

$$\boldsymbol{d}_k^{[j]} = \boldsymbol{y}_k^{[j]} - g^{[j]}(\hat{\boldsymbol{x}}_{k|k-1}^{[j]}) \tag{16}$$

$$\boldsymbol{S}_k^{[j]} = \boldsymbol{G}_k^{[j]} \boldsymbol{P}_{k-1|k-1}^{[j]} (\boldsymbol{G}_k^{[j]})^T + \boldsymbol{R}_k^{[j]} \tag{17}$$

Where c represents the normalized coefficient, and $\Lambda_k^{[j]}$ represents the maximum likelihood function.

Step 4: Output interaction

The final step of the IMM algorithm is the interaction of the output. In simple terms, the estimated values of the filtering results of all the models obtained in the previous three steps are weighted by the model probability function to obtain the total state estimation value $\hat{\boldsymbol{x}}_{k|k}$ and covariance estimation value $\boldsymbol{P}_{k|k}$ of the current cycle. Specifically, the total state estimation $\hat{\boldsymbol{x}}_{k|k}$ and the covariance estimation $\boldsymbol{P}_{k|k}$ are calculated as follows:

$$\hat{\boldsymbol{x}}_{k|k} = \sum_{j=1}^{M} \hat{\boldsymbol{x}}_{k|k}^{[j]} \boldsymbol{\mu}_k^{[j]} \tag{18}$$

$$\boldsymbol{P}_{k|k} = \sum_{j=1}^{M} \boldsymbol{\mu}_k^{[j]} \cdot [\boldsymbol{P}_{k|k}^{[j]} + (\hat{\boldsymbol{x}}_{k|k}^{[j]} - \hat{\boldsymbol{x}}_{k|k}) \cdot (\hat{\boldsymbol{x}}_{k|k}^{[j]} - \hat{\boldsymbol{x}}_{k|k})^T] \tag{19}$$

At this juncture, the existing recursive loop calculation is concluded. The total state estimation value $\hat{\boldsymbol{x}}_{k|k}$ and the covariance estimation value $\boldsymbol{P}_{k|k}$ of the current loop will be calculated as the initial value of input interaction in the subsequent loop. This allows for the continuous adjustment of the model's weight by the uncertainty of the current observation and state estimation, thereby facilitating more precise state estimation and prediction.

3.2. Sensorless control observer design based on IMM-EKF algorithm

The algorithmic flow of IMM-EKF has been previously detailed in the preceding section. It is no longer described too much here. The core idea of the IMM-EKF algorithm is to combine multiple models (linear or nonlinear) to form a hybrid model and use the weighted average method to fuse them to achieve better estimation results. Among them, the input model interaction and new data fusion are the main differences between the IMM-EKF algorithm and the single model filter algorithm. The main advantage of the IMM-EKF algorithm is that it can deal with non-linear, non-Gaussian systems, and can use multiple different motion models to describe the motion of the system, thereby improving the accuracy of the estimation. In addition, the IMM-EKF algorithm can also adaptively adjust the weight of each EKF filter according to different requirements and actual conditions to adapt to different working conditions.

As previously stated, the nonlinear nature of the motor system necessitates linearization. The processed system state equation is as follows:

$$\begin{cases} \boldsymbol{x}_{k+1} = F(\boldsymbol{x}_k, \boldsymbol{u}_k) + \boldsymbol{q}_k \\ \boldsymbol{y}_k = G(\boldsymbol{x}_k) + \boldsymbol{r}_k \end{cases} \tag{20}$$

Where both $\boldsymbol{q}_k$ and $\boldsymbol{r}_k$ are random zero-mean Gaussian white noise introduced by discretization. The former represents the system noise and is related to the accuracy of the system. The latter represents the measurement noise and is related to the accuracy of the controller measurement data.

The state variable $\boldsymbol{x}_k$ and the state space transformation equation $F(\boldsymbol{x}_k,\boldsymbol{u}_k)$ are shown as follows.

$$\boldsymbol{x}_k = \begin{bmatrix} i_{d,k} & i_{q,k} & R_{s,k} & V_{dead,k} & L_{s,k} & \psi_{s,k} \end{bmatrix}^T \tag{21}$$

Metrol. Meas. Syst., Vol. 32 (2025), No. 2
DOI: 10.24425/mms.2025.154339

$$F(\boldsymbol{x}_k,\boldsymbol{u}_k)=\begin{bmatrix}\left(1-\dfrac{R_{s,k}}{L_{n,k}}T_s\right)i_{d,k}+\omega_{e,k}i_{q,k}T_s+\dfrac{u_{d,k}^{*}-V_{dead,k}D_{d,k}}{L_d}T_s\\ \left(1-\dfrac{R_{s,k}}{L_{n,k}}T_s\right)i_{q,k}-\omega_{e,k}i_{d,k}T_s+\left(\dfrac{u_{q,k}^{*}-V_{dead,k}D_{q,k}}{L_{n,k}}-\dfrac{\psi_{m,k}}{L_{n,k}}\omega_{e,k}\right)T_s\\ R_{s,k}\\ V_{dead,k}\\ L_{s,k}\\ \psi_{s,k}\end{bmatrix} \tag{22}$$

Four models are selected to describe the motion state of sensorless control considering parameter identification and inverter nonlinearity. The state variables of each model are as follows:

$$\boldsymbol{x}^{[1]}=\begin{bmatrix}i_d\\ i_q\\ \omega_e\\ V_{dead}\\ 0\\ 0\\ 0\end{bmatrix},\ \boldsymbol{x}^{[2]}=\begin{bmatrix}i_d\\ i_q\\ \omega_e\\ 0\\ R_s\\ 0\\ 0\end{bmatrix},\ \boldsymbol{x}^{[3]}=\begin{bmatrix}i_d\\ i_q\\ \omega_e\\ 0\\ 0\\ L_s\\ 0\end{bmatrix},\ \boldsymbol{x}^{[4]}=\begin{bmatrix}i_d\\ i_q\\ \omega_e\\ 0\\ 0\\ 0\\ \psi_s\end{bmatrix} \tag{23}$$

Each sub-model selected in this way only identifies one parameter while estimating the motor speed, which satisfies the observability discrimination and can ensure the observability and reliability of the estimated parameters.

For each submodel:

$$F_{k-1}^{[j]}=F_{Jacobi}^{[j]}=\frac{\partial F^{[j]}(\hat{\boldsymbol{x}}_{k-1|k-1}^{[j]},u_k^{[j]})}{\partial\hat{\boldsymbol{x}}_{k-1|k-1}^{[j]}} \tag{24}$$

$$G_{k-1}^{[j]}=G_{Jacobi}^{[j]}=\frac{\partial G^{[j]}(\hat{\boldsymbol{x}}_{k-1|k-1}^{[j]})}{\partial\hat{\boldsymbol{x}}_{k-1|k-1}^{[j]}} \tag{25}$$

$$\boldsymbol{Q}^{[j]}=\mathrm{cov}(\boldsymbol{q}_k^{[j]}),\ \boldsymbol{R}^{[j]}=\mathrm{cov}(\boldsymbol{r}_k^{[j]}) \tag{26}$$

Where $\boldsymbol{Q}$ and $\boldsymbol{R}$ are the noise covariance matrix of the system noise of model j and the covariance matrix of the measurement noise, respectively, which are usually selected according to the model noise and debugging experience.

4. Simulation analysis and experimental verification

4.1. Simulation analysis

To verify the feasibility and effectiveness of the proposed algorithm, the simulation model of this paper is built in MATLAB/SIMULINK based on the accurate modeling model of vector control and the principle block diagram of the IMM-EKF algorithm in Fig. 2. Some of the module parameters of the model are shown in Table 1.

Table 1. Motor and power device parameters

Category	Parameter name	Parameter value
Electrical machine	Rated power, P	0.75 kW
	Rated voltage, U_{dc}	310 V
	Rated current, I	7.2 A
	Rated speed, N_r	3000 r/min
	Rated torque, T	2.4 Nm
	Line back electromotive force, E	49.3% V/(10^3r·min^{-1})
	Rotor inertia, J	1.4±10% (kg·m^2·10^{-4})
	Stator resistance, R	1.176±10% Ω
	Inductance, L	9.5±10% mH
	Permanent magnet flux, Ψ_f	0.0485 wb
	Pole pairs, N_p	5
Power device	Turn-off delay time, T_{off}	40 ns(25°C)
	Turn-on delay time, T_{on}	35 ns(25°C)
	Switching frequency, T_{PWM}	10 kHz
	Dead time, T_{dead}	2 μs

To verify the feasibility and effectiveness of the sensorless control algorithm with compensation proposed in this paper, a 20% rated load is applied at 500 r/min and 1000 r/min, and the simulation analysis of compensation effect and sensorless estimation is carried out. The specific analysis results are as follows:

By comparing Fig. 3(a), (c), (e) and (b), (d), (f), it can be found that compared with Fig. 3(a), the stator current waveform of Fig. 3(b) with the proposed dead-time compensation algorithm is significantly improved, and the current clamping phenomenon and current waveform distortion caused by inverter nonlinearity are significantly reduced. Through the frequency domain analysis of the current waveforms of Fig. 3(a) and (b), Fig. 3(c), (e) and (d), (f) can be obtained. By comparing the frequency domain analysis of the current before and after compensation, it can be clearly found that the amplitude of the 5th and 7th harmonic components in the *a*-phase current and the amplitude of the 6th harmonic component in the *dq*-axis current are greatly reduced. The result is that the sinusoidality of the circuit waveform becomes better, and the current improvement after compensation is more obvious.

In terms of sensorless control performance, as shown in Fig. 4(a)-(h), the speed and angle estimation analysis of the proposed sensorless algorithm under 500 r/min and 20% load are performed before and after compensation, respectively. Observing the group diagram after compensation, it can be found that the estimated speed and estimated angle after compensation not only converge to the actual value, but also the estimated speed error is about 20 r/min. At this time, the relative estimation error of the speed is about 4%, and the estimation accuracy is improved by about 60% compared with that before compensation.

The simulation analysis under high speed and light load conditions is shown in Fig.5 and Fig.6, which are the current and current frequency domain analysis group diagram before and after compensation under 1000 r/min and 20% load, and the estimated speed and estimated angle analysis group diagram before and after compensation. It can be seen from Fig.5 and Fig.6 that the sinusoidal characteristics of the current waveform before and after compensation are greatly improved, and the amplitude of the current harmonic component caused by the nonlinearity of the inverter is also reduced accordingly. The proposed algorithm also has a good compensation effect under high speed and light load. Under the condition of high speed and light load, the speed estimation error and angle estimation error are also much smaller than those before compensation. The simulation results show that the proposed algorithm has good compensation and estimation ability under this condition.

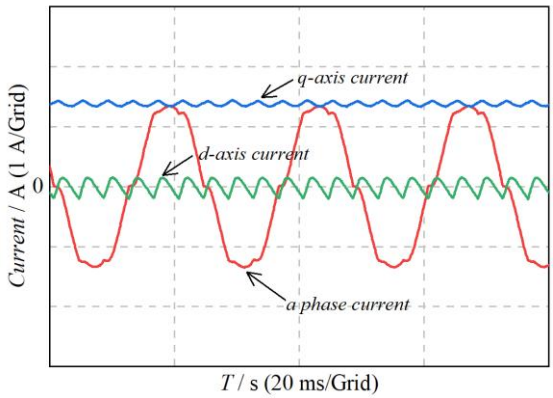

(a) Current waveform before compensation

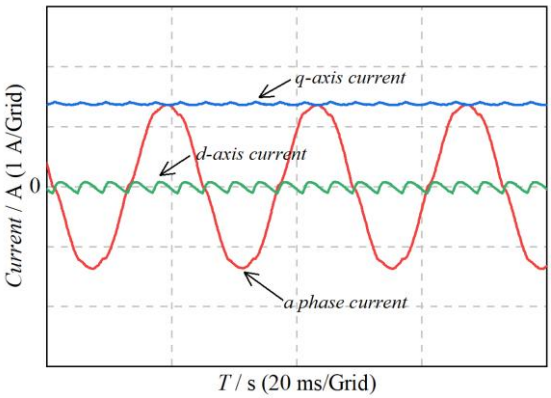

(b) Current waveform after compensation

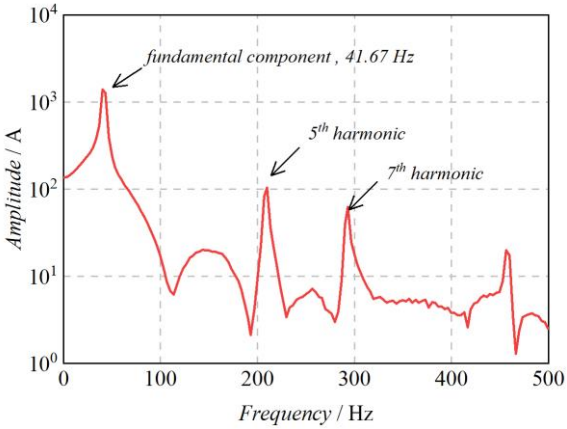

(c) *a* phase current before compensation

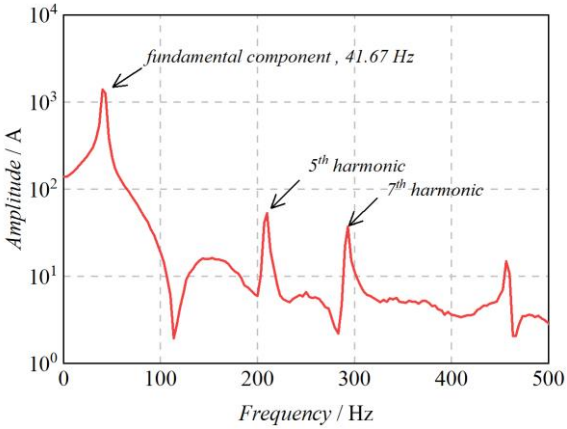

(d) *a* phase current after compensation

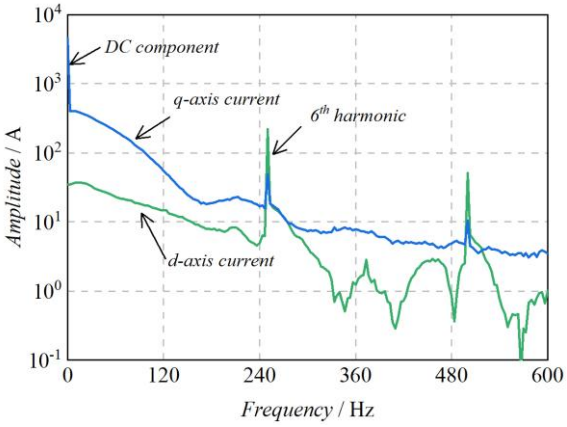

(e) *dq* axis current before compensation

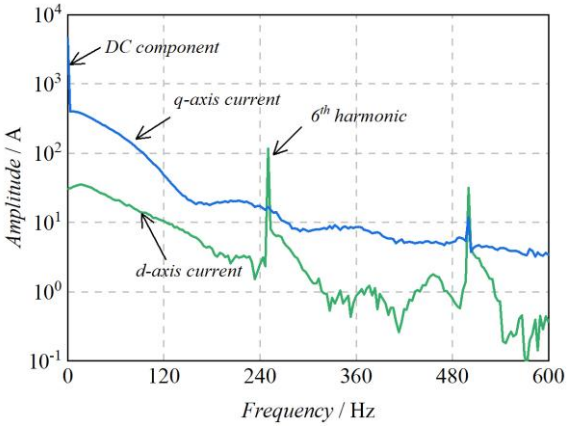

(f) *dq* axis current after compensation

Fig. 3. Current waveform and current frequency domain analysis before and after compensation at 500 r/min

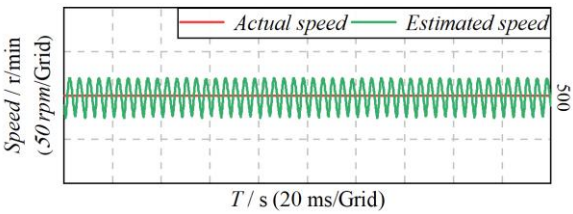

(a) Speed waveform before compensation

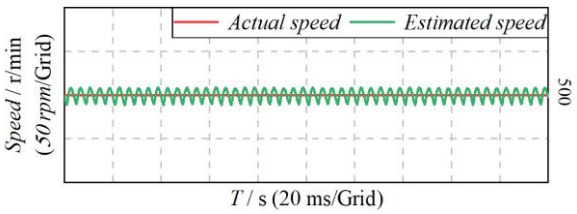

(b) Speed waveform after compensation

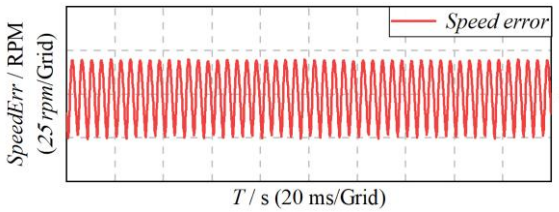

(c) Speed error waveform before compensation

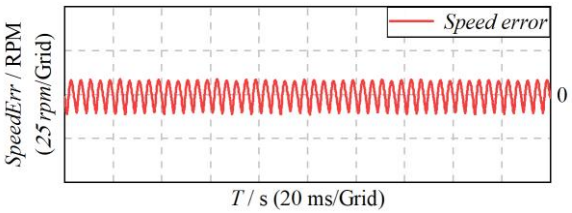

(d) Speed error waveform after compensation

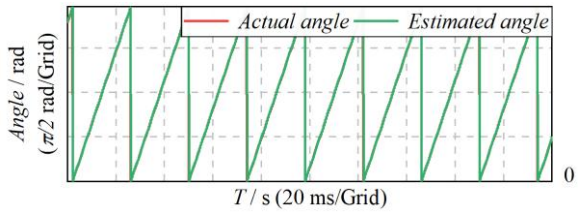

(e) Angle waveform before compensation

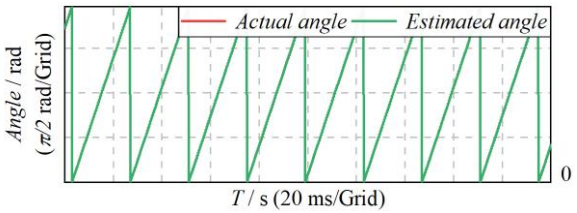

(f) Angle waveform after compensation

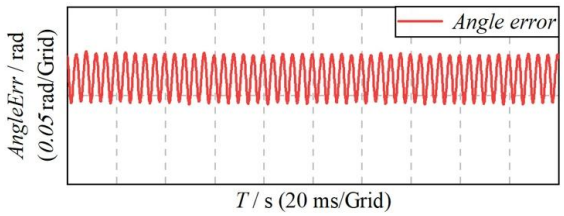

(g) Angle error waveform before compensation

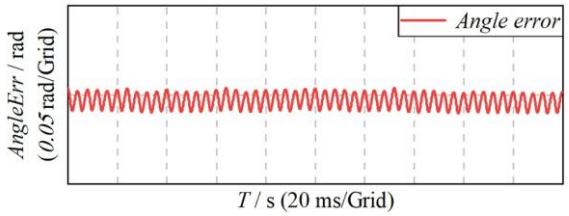

(h) Angle error waveform after compensation

Fig. 4. Analysis of speed and angle before and after compensation at 500 r/min

Metrol. Meas. Syst., Vol. 32 (2025), No. 2
DOI: 10.24425/mms.2025.154339

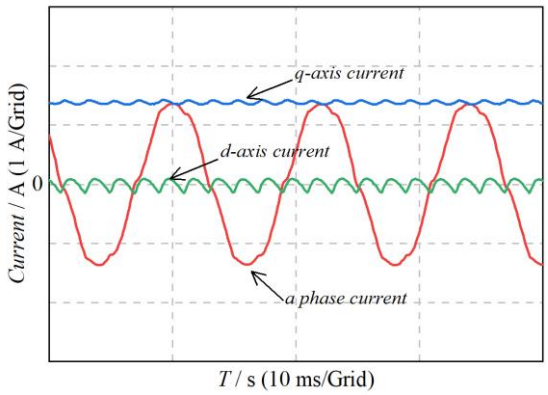

(a) Current waveform before compensation

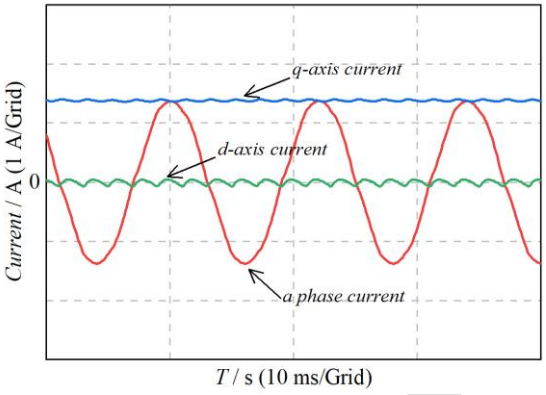

(b) Current waveform after compensation

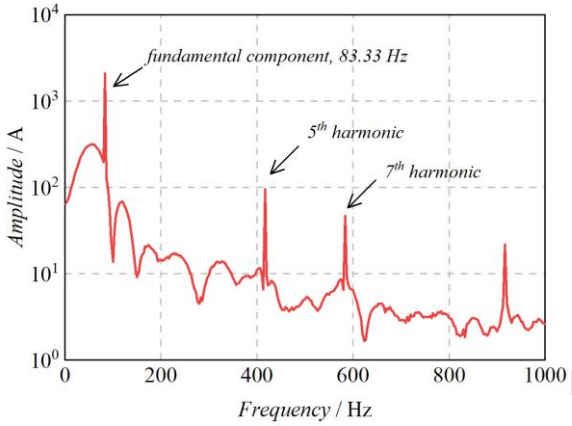

(c) *a* phase current before compensation

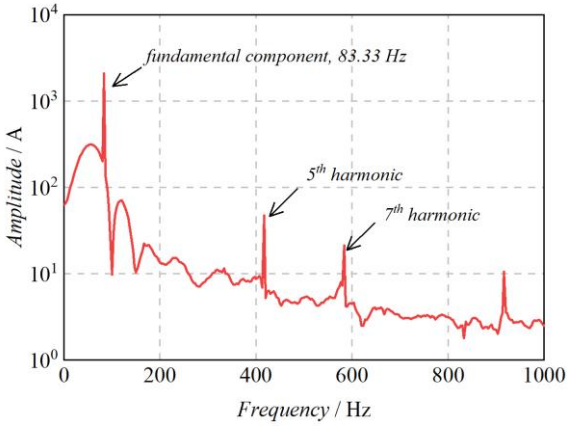

(d) *a* phase current after compensation

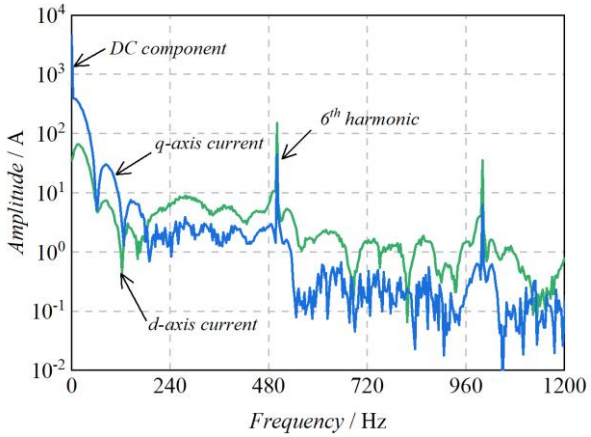

(e) *dq* axis current before compensation

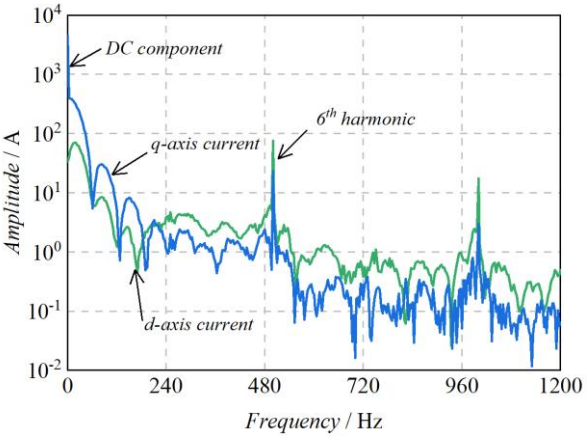

(f) *dq* axis current after compensation

Fig. 5. Current waveform and current frequency domain analysis before and after compensation at 1000 r/min

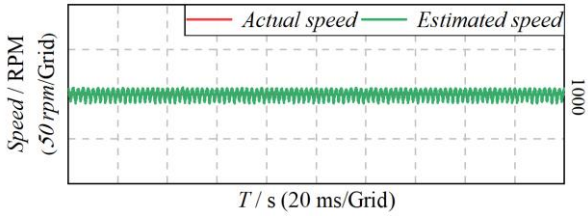

(a) Speed waveform before compensation

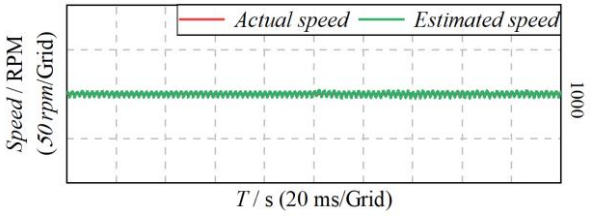

(b) Speed waveform after compensation

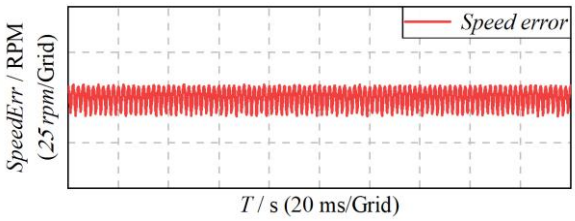

(c) Speed error waveform before compensation

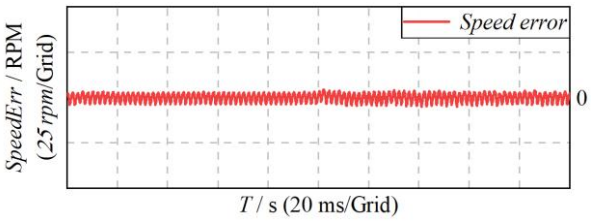

(d) Speed error waveform after compensation

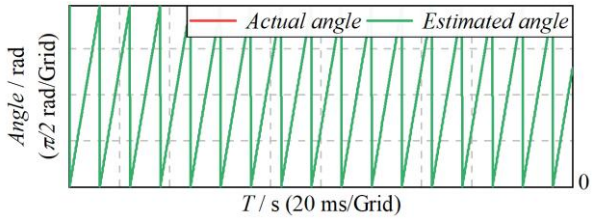

(e) Angle waveform before compensation

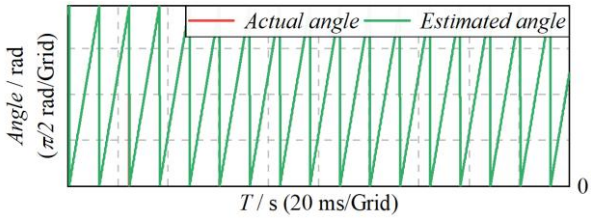

(f) Angle waveform after compensation

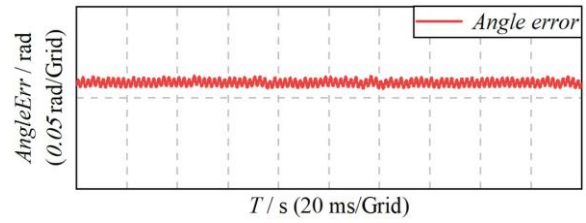

(g) Angle error waveform before compensation

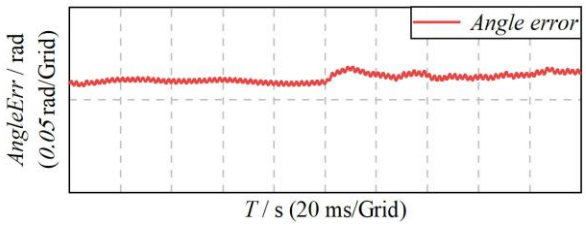

(h) Angle error waveform after compensation

Fig. 6. Analysis of speed and angle before and after compensation at 1000 r/min

4.2. Experimental verification

The experiment is carried out on the two-motor dragging test bench shown in Fig. 7. The experimental motor parameters used in the experiment are consistent with the motor parameters used in the simulation analysis, as shown in Table 1.

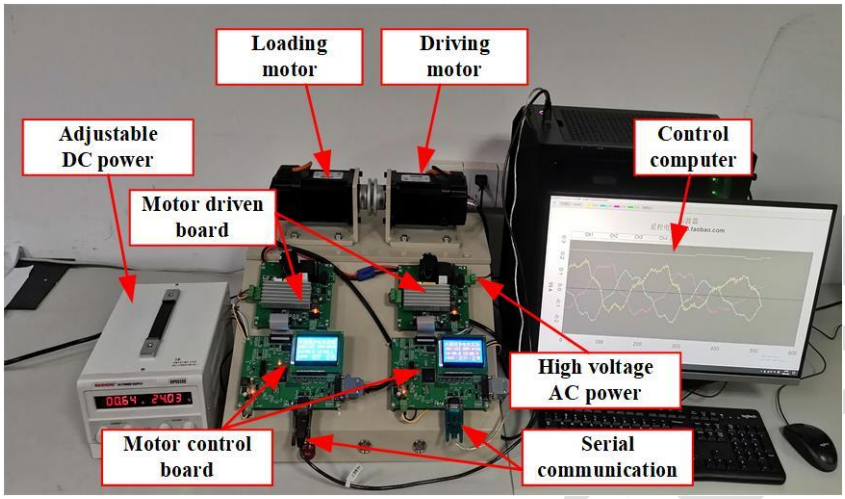

Fig. 7. The physical diagram of the motor experimental bench

Fig. 8 shows the hardware frame structure diagram of the dual-motor dragging test bench. The driving circuit board is a high-voltage component composed of a rectifier circuit, an inverter circuit, and a current and voltage sampling circuit. The control board is in the low-voltage part. This part mainly includes the main control chip, reset circuit, crystal oscillator circuit, *etc.* The main control part selects the DSP chip of TMS320F28335 as the main computing CPU. Its operation speed is as high as 150 MHz, and it has an FPU floating-point operation unit, which is responsible for signal acquisition, various algorithm implementations, and PWM signal output.

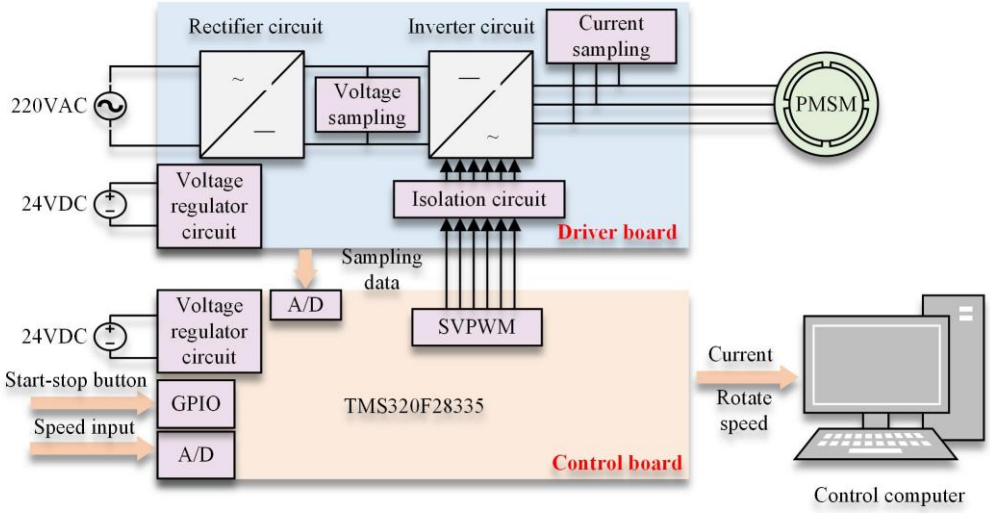

Fig. 8. Block diagram of the test bench hardware

In this paper, the following methods are used to verify the proposed control algorithm. In the CCS compilation environment, the drive system runs the IMM-EKF algorithm scheme. During the execution of the scheme, the program can also be uploaded to the PC using a serial port, and communicate with the PC to send information such as current and speed. In the loading

system, the torque output program allows the PC to select the dynamic and static load torque curves and input them to the loading control system through a serial interface to apply the load.

As shown in Fig. 9 and Fig. 10, the current waveform diagram and the estimated speed and estimated angle analysis diagram are shown under the acceleration and deceleration conditions of the initial speed of 500 r/min, 20% rated load constant speed load running for 0.3 s, the sudden speed to 2000 r/min and then reduced to 500 r/min. Fig. 9 shows the current waveform under the acceleration and deceleration conditions. At this time, the burrs in the *dq* axis except for noise are reduced, and the waveform is smoother under a steady state. The sinusoidal characteristics of the *a*-phase current waveform are better. The zero-point clamping phenomenon and current distortion caused by the dead zone are close to the current waveform after simulation improvement. According to the comprehensive observation of Fig. 10, it can be found that the proposed sensorless control algorithm converges well with the reference value in estimating the speed and angle, and fluctuates up and down near it. At the steady-state speed of 500 r/min, the estimation error is about 25 r/min, and the relative estimation error of the speed is about 5%. At 2000 r/min steady-state speed, the estimation error is about 10 r/min, and the relative estimation error of speed is about 0.5%. When the speed changes abruptly, the estimated speed still tracks the actual value well, and the estimated speed error is very small during acceleration and deceleration. Therefore, it can be proved that the proposed algorithm has better anti-speed disturbance ability.

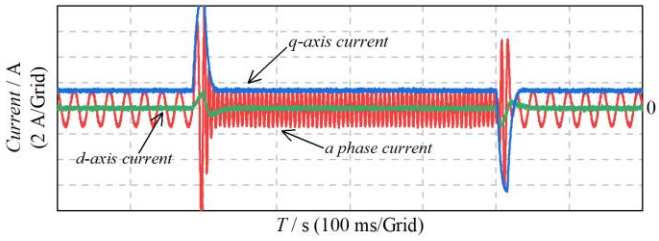

Fig. 9. Variable speed stator current waveforms

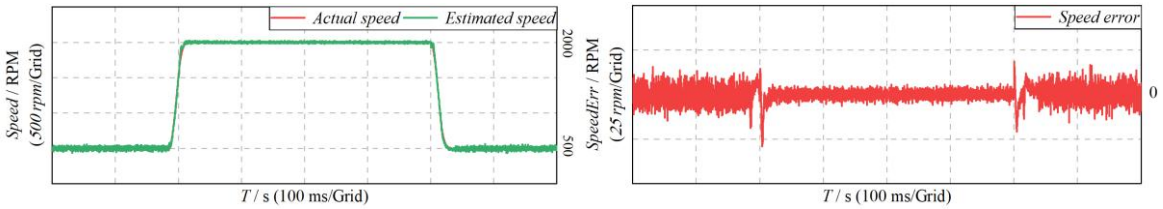

(a) Estimate speed waveform (b) Estimate the speed error waveform

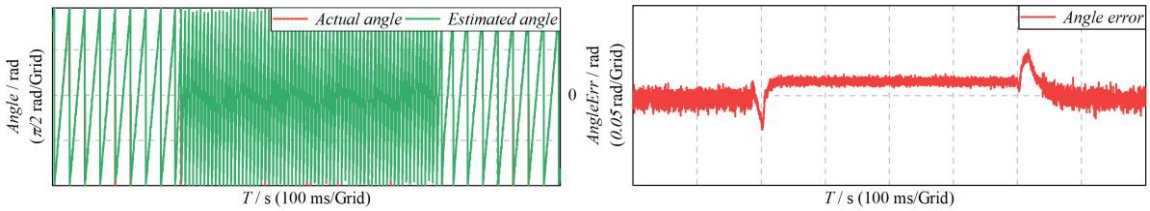

(c) Estimate angle waveform (d) Estimate angle error waveform

Fig. 10. Estimated speed and angle analysis under acceleration and deceleration conditions

As shown in Fig. 11 and Fig. 12, the current waveform diagram and the estimated speed and angle analysis diagram under the loading and unloading conditions of the initial speed of 500 r/min, 20% rated load constant speed load operation of 0.3 s, sudden load of 80%, and then reduced to 20% rated load. Since the current frequency domain analysis cannot be carried out under unsteady conditions, only the current waveform and the estimated speed and estimated

angle are analyzed and displayed under this condition. Fig. 11 shows the current waveform under the loading and unloading conditions. At this time, the burrs in the *dq* axis except for noise are reduced, the waveform is smoother under a steady state, the sine of the *a*-phase current waveform is better, and the zero-point clamping phenomenon and current distortion caused by the dead zone are improved. It can be seen from Fig. 12 that the proposed sensorless control algorithm converges well to the reference value in the estimated speed and estimated angle, and fluctuates up and down near it. The speed estimation error is about 25 r/min under the steady state of 500 r/min low load, and the relative estimation error is about 5 %. Under the steady state of 500 r/min low speed and high load, the speed estimation error is reduced by about 15 r/min, and the relative error is about 3%. The identification accuracy is superior under high load steady state. Under low load steady state and high load steady state, the angle estimation error does not exceed 0.02 rad. When the torque changes abruptly, the estimated speed and estimated angle still track the actual value well, and the estimated speed error and estimated angle error are very small during loading and unloading. Therefore, it can be proved that the proposed algorithm has better anti-load disturbance ability.

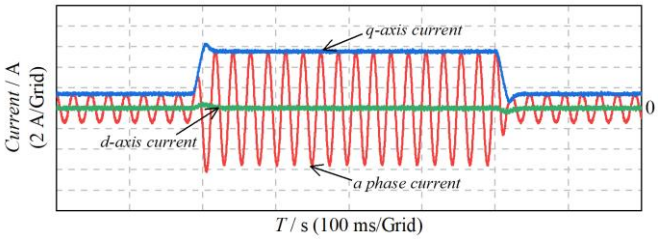

Fig. 11. Variable load stator current waveforms

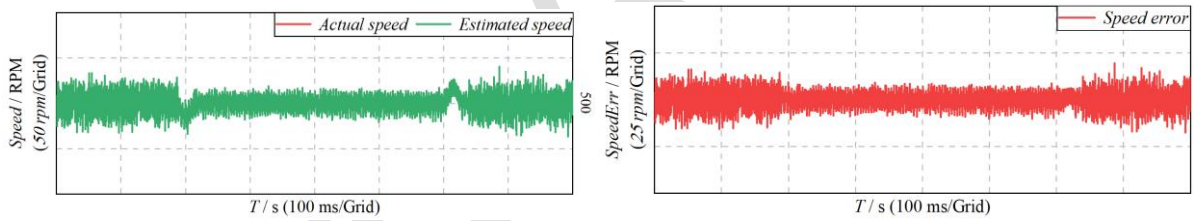

(a) Estimate speed waveform

(b) Estimate the speed error waveform

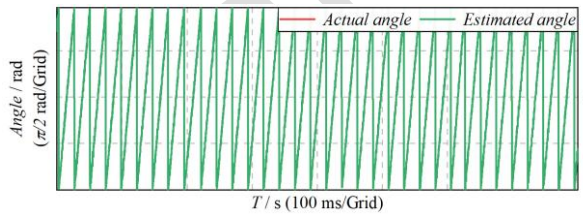

(c) Estimate angle waveform

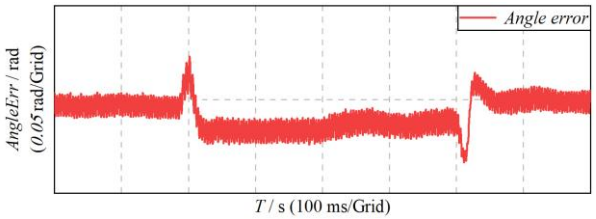

(d) Estimate angle error waveform

Fig. 12. Estimated speed and angle analysis under variable torque conditions

5. Conclusions

In this paper, an interactive multi-model extended Kalman filter position sensorless control algorithm is proposed. The algorithm exhibits high speed and angle identification accuracy, a smooth current waveform, and robust performance. In the face of variable speed, the estimated speed and estimated angle have small fluctuation, fast convergence speed, and good anti-disturbance ability. This paper is limited in that it does not address the estimation problem at

zero speed. In future work, the switching strategy for zero-low speed and medium-high speed will be studied to realize composite sensorless control across the full speed range.

Acknowledgements

This work was supported by the National Key R&D Program of China (Grant number 2021YFB2501700), the National Natural Science Foundation of China (Grant number 51705213) and the State Key Laboratory of Intelligent Green Vehicle and Mobility (Grant No. KFY2409).

References

[1] Zhu, J., Nan, H., & Guo, X. (2024). Design and analysis of a novel three-segment Halbach permanent magnet array coreless AFPMG. *Journal of Jiangsu University (Natural Science Edition), 45*(1), 105–111. https://doi.org/10.3969/j.issn.1671-7775.2024.01.015 (in chinese)

[2] Boyar, A., Kabalci, E., & Kabalci, Y. (2024). Sensorless speed controller of an induction motor with MRAS-based model predictive control. *Computers and Electrical Engineering, 118*, 109350. https://doi.org/10.1016/j.compeleceng.2024.109350

[3] Li, J., Feng, B., & Li, S. (2023). Speed control of permanent magnet synchronous motor based on RESO and composite sliding mode. *Journal of Jiangsu University (Natural Science Edition), 44*(3), 330–336. https://doi.org/10.3969/j.issn.1671-7775.2023.03.012 (in Chinese)

[4] Yang, M., Li, S., & Li, Z. (2022). Active disturbance rejection controller of direct torque for permanent magnet synchronous motor based on super-twisting sliding mode. *Journal of Jiangsu University (Natural Science Edition), 43*(6), 680–684. https://doi.org/10.3969/j.issn.1671-7775.2022.06.009 (in chinese)

[5] Sun, L. (2022). Low speed sensorless control method of brushless DC motor based on pulse high frequency voltage injection. *Alexandria Engineering Journal, 61*(8), 6457–6463. https://doi.org/10.1016/j.aej.2021.12.005

[6] Wang, G., Valla, M., & Solsona, J. (2019). Position sensorless permanent magnet synchronous machine drives—A review. *IEEE Transactions on Industrial Electronics, 67*(7), 5830–5842. https://doi.org/10.1109/TIE.2019.2955409

[7] Sun, X., Zhang, Y., Tian, X., Cao, J., & Zhu, J. (2021). Speed sensorless control for IPMSMs using a modified MRAS with gray wolf optimization algorithm. *IEEE Transactions on Transportation Electrification, 8*(1), 1326–1337. https://doi.org/10.1109/TTE.2021.3093580

[8] Sun, X., Cai, F., Yang, Z., & Tian, X. (2022). Finite position control of interior permanent magnet synchronous motors at low speed. *IEEE Transactions on Power Electronics, 37*(7), 7729–7738. https://doi.org/10.1109/TPEL.2022.3146841

[9] Li, T., & Zhou, J. (2018). High-stability position-sensorless control method for brushless DC motors at low speed. *IEEE Transactions on Power Electronics, 34*(5), 4895–4903. https://doi.org/10.1109/TPEL.2018.2863735

[10] Zhang, Z. (2022). Sensorless back EMF based control of synchronous PM and reluctance motor drives—A review. *IEEE Transactions on Power Electronics, 37*(9), 10290–10305. https://doi.org/10.1109/TPEL.2022.3162963

[11] Marchesoni, M., Passalacqua, M., Vaccaro, L., Calvini, M., & Venturini, M. (2020). Performance improvement in a sensorless surface-mounted PMSM drive based on rotor flux observer. *Control Engineering Practice, 96*, 104276. https://doi.org/10.1016/j.conengprac.2019.104276

[12] Boztas, G., & Aydogmus, O. (2022). Implementation of sensorless speed control of synchronous reluctance motor using extended Kalman filter. *Engineering Science and Technology, an International Journal, 31*, 101066. https://doi.org/10.1016/j.jestch.2021.09.012

[13] Gamazo-Real, J. C., Martínez-Martínez, V., & Gomez-Gil, J. (2022). ANN-based position and speed sensorless estimation for BLDC motors. *Measurement, 188*, 110602. https://doi.org/10.1016/j.measurement.2021.110602

[14] Zhang, W., Zhang, Z., Lu, J., Chen, T., & Li, Y. (2023). Back electromotive force-based discrete-time rotor position bias compensation method for permanent magnet synchronous motors. *IEEE Transactions on Power Electronics, 38*(10), 13030–13041. https://doi.org/10.1109/TPEL.2023.3298213

[15] Ye, S. (2019). Design and performance analysis of an iterative flux sliding-mode observer for the sensorless control of PMSM drives. *ISA Transactions, 94*, 255–264. https://doi.org/10.1016/j.isatra.2019.04.009

[16] Yang, Z., Ding, Q., Sun, X., Lu, C., & Zhu, H. (2022). Speed sensorless control of a bearingless induction motor based on sliding mode observer and phase-locked loop. *ISA Transactions, 123*, 346–356. https://doi.org/10.1016/j.isatra.2021.05.041

[17] İnan, R., Aksoy, B., & Salman, O. K. M. (2023). Estimation performance of the novel hybrid estimator based on machine learning and extended Kalman filter proposed for speed-sensorless direct torque control of brushless direct current motor. *Engineering Applications of Artificial Intelligence, 126*, 107083. https://doi.org/10.1016/j.engappai.2023.107083

[18] Lu, J., Hu, Y., Zhang, X., Wang, Z., Liu, J., & Gan, C. (2018). High-frequency voltage injection sensorless control technique for IPMSMs fed by a three-phase four-switch inverter with a single current sensor. *IEEE/ASME Transactions on Mechatronics, 23*(2), 758–768. https://doi.org/10.1109/TMECH.2018.2803772

[19] Wang, Y., Xu, Y., & Zou, J. (2020). Online multiparameter identification method for sensorless control of SPMSM. *IEEE Transactions on Power Electronics, 35*(10), 10601–10613. https://doi.org/10.1109/TPEL.2020.2974870

[20] Kivanc, O. C., Ozturk, S. B., & Toliyat, H. A. (2022). On-line dead time compensator for PMSM drive based on current observer. *Engineering Science and Technology, an International Journal, 25*, Article 100987. https://doi.org/10.1016/j.jestch.2021.04.006

[21] Wang, Y., Xu, Y., & Zou, J. (2019). Sliding-mode sensorless control of PMSM with inverter nonlinearity compensation. *IEEE Transactions on Power Electronics, 34*(10), 10206–10220. https://doi.org/10.1109/TPEL.2018.2890564

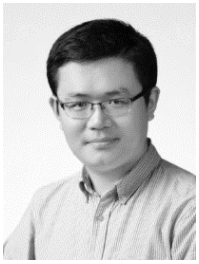

Yong Li is currently an associate professor with the Automotive Engineering Research Institute, Jiangsu University, China. He once studied at the University of Waterloo, Ontario, Canada. He has published more than 30 papers. His research interests include motor control and drive, vehicle system dynamics, complex electromechanical coupling systems.

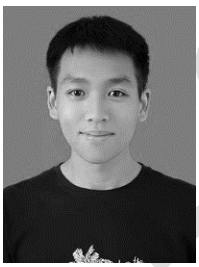

Jiexin An received the B.S. degree in vehicle engineering from the Zhengzhou University of Aeronautics, Henan Province, China, in 202l. He is currently pursuing the master's degree in vehicle engineering at Jiangsu University, Zhenjiang, China. His current research interests include simultaneous localization and mapping, motor control, and robot trajectory planning.

Han Hu received the B.S. degree in vehicle engineering from Huaiyin Institute of Technology, Huaian, Jiangsu Province, China, in 2020. He is currently working toward the master's degree in vehicle engineering with Jiangsu university, Zhenjiang, China. His current research interests include motor parameter identification and sensorless control.

Xing Xu received the B.Sc. degree in automotive engineering, the M.Sc. degree in control theory and control engineering, and the Ph.D. degree in agricultural electrification and automation from Jiangsu University, Zhenjiang, China, in 2002, 2006 and 2010, respectively. He is currently a Professor with the Automotive Engineering Research Institute, Jiangsu University. His research interests include the modeling, identification, optimization, fault diagnosis, and control of vehicle dynamic systems.